Computational and Experimental Studies of Electrohydrodynamic Atomization for Pharmaceutical Particle Fabrication

Alireza Rezvanpour, Eldin Wee Chuan Lim, and Chi-Hwa Wang
Dept. of Chemical and Biomolecular Engineering, National University of Singapore,
4 Engineering Drive 4, Singapore 117576, Singapore

DOI 10.1002/aic.13727
Published online in Wiley Online Library (wileyonlinelibrary.com).

Electrohydrodynamic atomization (EHDA) is a promising method for the fabrication of micro- and nanosized particles with narrow-size distribution and better morphologies in comparison to conventional methods of particle fabrication. A computational model was developed in this study to simulate the fluid and particle dynamics in an EHDA chamber, and thereby providing a means of predicting particle collection efficiencies at various operating conditions. Experiments were also conducted using a new design of the EHDA chamber. It was found that nitrogen flow rate, solution flow rate and voltage difference between the nozzle and ring can significantly affect the particle collection efficiency of the EHDA process. Electric field and electric potential profiles in the chamber were significantly affected by the combined voltages of the nozzle and ring. In general, a good qualitative agreement in particle collection efficiencies was obtained from experiments and simulations. The computational model developed in this study provided a means of understanding the various processes involved in micro- and nano-sized particle fabrication using the EHDA methodology. © 2012 American Institute of Chemical Engineers *AIChE J,* 00: 000–000, 2012

Keywords: electrohydrodynamic atomization, particle collection efficiency, particle trajectory, Lagrangian approach, simulation

Introduction

Electrohydrodynamic atomization (EHDA) is a well-established methodology for production of fine liquid droplets of uniform sizes. It has been demonstrated to be useful for fabricating particles with better morphologies than other conventional methods such as spray drying.[1–2] With controlled solvent evaporation during the particle fabrication process, further enhancements in terms of narrow polydispersities and smooth, spherical morphologies of particles can be achieved.[3] The underlying concept of electrohydrodynamic atomization is in the application of an electric field to a liquid that is flowing out of a capillary tube so as to induce hydrodynamic instabilities in the liquid stream which then gives rise to the phenomenon of atomization. As such, the electric potential difference applied needs to be sufficiently high in order to generate a strong electric field which is responsible for inducing instability within the liquid stream before atomization occurs. Both physical properties and operating conditions such as the electrical conductivity, surface tension, viscosity, flow rates and surrounding gas play important roles in determining the onset of hydrodynamic instabilities in liquids flowing through capillary tubes.[4] In the EHDA process, such physical properties also have significant effects on the formation of the liquid cone.[5] The formation of a stable liquid cone is essential for operation in the cone-jet mode which produces droplets that are roughly one order of magnitude smaller than the diameter of the capillary tube.[6–10]

Apart from experimental studies, various aspects of the EHDA process have been investigated computationally. An air-assisted electrostatic induction charging spray nozzle was modeled for both flat and spherical targets.[11] The airflow, liquid droplets as well as the electrostatic field were considered for calculation of trajectories of the charged droplets. The effects of parameters such as droplet size, charge-to-mass ratio and nozzle-to-target distance on the motion of the charged droplets were investigated. The results confirmed that the spray cloud expanded with increasing droplet charge-to-mass ratio and nozzle-to-target distance due to increasing space charge.[11] Nonlinear breakup of charged liquid jets was analyzed numerically in the limit of very small electrical Strouhal numbers $T_e/T_b << 1$ (i.e., negligible charge relaxation effects, applicable to highly conducting liquids), where T_e is the electric relaxation time of charges, and T_b is the breakup time in a Lagrangian framework following the liquid jet at its average axial velocity.[7] The influence of the electrical Bond's number and viscosity on the capillary Rayleigh's most probable breakup length, the breakup time, the volume of the satellite, and the charge of both main drop and satellite were analyzed. The electrical Bond's number is a dimensionless number expressing the ratio of body forces (electric forces) to surface tension forces.

Correspondence concerning this article should be addressed to C.-H. Wang at chewch@nus.edu.sg.

© 2012 American Institute of Chemical Engineers

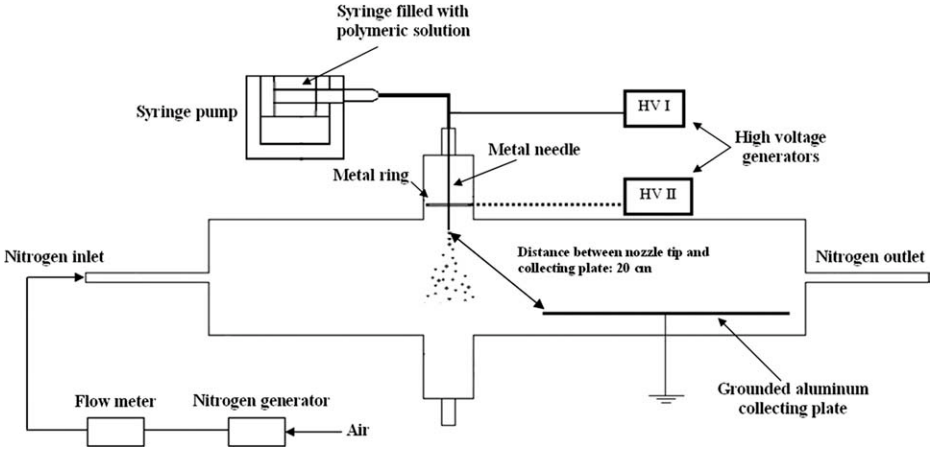

Figure 1. Experimental setup for the EHDA process.

The findings confirmed that the influence of the electrical Bond's number on Rayleigh's length was small within the usual parametric limits of stability of a steady Taylor cone-jet at atmospheric pressure.[7] The commercial computational fluid dynamics (CFD) software known as CFX 4.4 had also been used to simulate the EHDA process.[8] The heat conduction equation was modified to represent the electrostatic field and electric body forces were determined during the calculations. The calculated velocity fields for an EHDA process using heptane and ethanol as the operating fluids were found to be consistent with published results. The model applied did not include a droplet breakup model but droplet size calculated based on jet diameter was found to compare well with experiments.[8] The atomization of water had also been studied both experimentally and computationally using CFD.[12] Based on the experimental results the atomization of water occurred outside the applicability range of the scaling laws due to the high-dielectric constant of water and the low-flow rate used. The experimental results also showed that droplet size remained approximately constant with increasing flow rate.[12] In other recent studies, the effects of various operating conditions such as electric field strength, liquid and inert gas-flow rate on particle size and morphology were reported.[13–16]

Particle collection efficiency is an important issue in particle fabrication using the EHDA process. Despite its importance, this aspect of the EHDA process has not been adequately addressed in the literature to date. As the materials used for pharmaceutical particle fabrication are expected to be expensive, high-particle collection efficiency is essential for the EHDA process to be operationally feasible. This work aims to employ the EHDA process as a method for micro- and nano-sized particle fabrication with a view toward understanding the effects of various operating parameters on the particle collection efficiency achievable with a new design of the EHDA chamber. CFD simulations of both particle and fluid phases within the EHDA chamber were carried out using FLUENT 6.3 and COMSOL 3.4. The simulation results obtained were validated against experimental data collected using an actual EHDA setup with the same geometry and applying the same operating conditions.

Experimental Methods

Electrohydrodynamic atomization (EHDA) process

In the experimental apparatus used in this study a nozzle (0.41 mm ID) and ring (40 mm ID) electrode were enclosed within a glass chamber (Figure 1). The distance between the nozzle and the ring was varied between 10–15 mm. The distance between the nozzle and the collecting plate was 200 mm. High-electric potential was applied to both the nozzle (7 kV–9 kV) and ring (5 kV– 7 kV) electrodes while the collecting plate that was made of aluminum was grounded.

The chamber used in this experiment was modified from the one used in previous studies.[16–18] The interior space of the chamber was 550 mm in length and 110 mm in diameter. The length of the inlet and outlet tube was 100 mm with a diameter of 15 mm. In comparison with the previous chamber designs, three major improvements can be identified in the current chamber design. First, the new chamber is entirely cylindrical while previous chambers used had two conical ends. Second, particles fabricated in the new chamber are collected inside the chamber itself and far away from the spray zone. Finally, the diameters of the inlet and outlet for nitrogen flow are larger than the previous designs. As will be seen in the simulation and experimental results in later sections of this article, these modifications had significant effects on the flow behaviors of both the inert gas (nitrogen), as well as the particles fabricated. Consequently, higher particle collection efficiencies and lower amounts of residual organic solvent in the collected particles were achieved.

The spray encapsulation section includes the nozzle-ring configuration and the surrounding space within the chamber. The nozzle and the ring electrodes were connected to two high-voltage DC power supplies independently (Glassman High Voltage, Inc., NJ, USA). These gave rise to the electric field within the chamber for the EHDA process. A high-positive electric potential relative to ground was applied to the nozzle, while a lower positive electric potential was applied to the ring. The ring was deployed to render better control of the EHDA spray, while the grounded plate acted as the counter-electrode to the nozzle and ring for discharging the collected particles. The distance between the nozzle and the collecting plate was larger than the distance mentioned in previous studies. This larger distance provided more time for evaporation of organic solvent from the droplets formed. A polymeric solution was pumped from a syringe into the chamber using a programmable syringe pump (Stoeting Co., IL, USA). An inert gas (nitrogen) was introduced from the left end of the chamber to transport particles formed from the liquid droplets to the collecting plate.

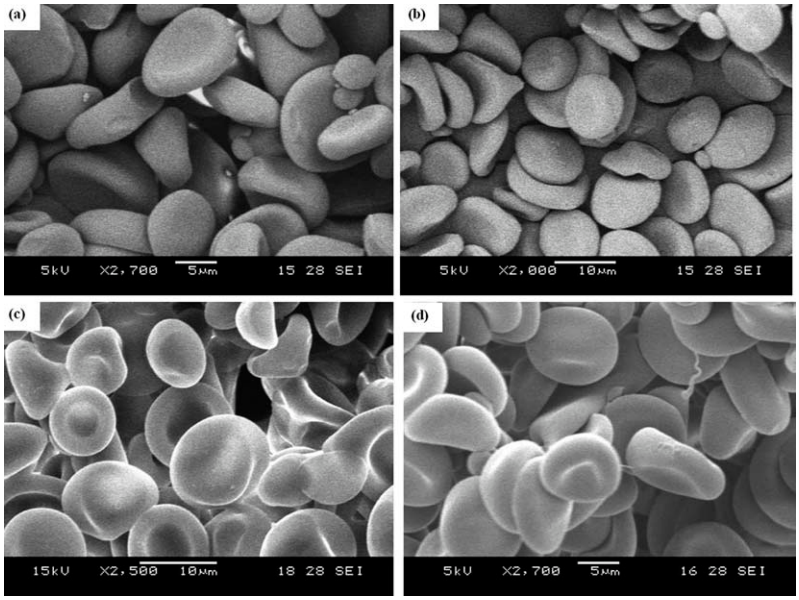

Figure 2. Pharmaceutical particles fabricated by the current EHDA process under the following conditions (a) nozzle voltage 7.5 kV, ring voltage 5.5 kV, Solution flow rate 2.5 mL/h and nitrogen flow rate 25 L/min, (b) nozzle voltage 8.5 kV, ring voltage 5.5 kV, Solution flow rate 1.5 mL/h and nitrogen flow rate 30 L/min, (c) nozzle voltage 8.5 kV, ring voltage 7 kV, solution flow rate 2.0 mL/h and nitrogen flow rate 25 L/min, and (d) nozzle voltage 7.5 kV, ring voltage 6 kV, solution flow rate 2.0 mL/h and nitrogen flow rate 20 L/min.

The cross-flow of inert gas was used inside the chamber to aid both the evaporation of the organic solvent from the droplets and the collection of the particles via a pneumatic conveying method. Due to the presence of high voltages, nitrogen was used as inert gas to minimize the possibility of sparks and combustion in the chamber. Figure 2 shows the morphology of pharmaceutical particles fabricated by the current EHDA process. It may be observed that discrete particles with biconcave shapes have been obtained.

Polymeric Solution

The polymeric solution used consisted of Poly(D, L-lactide-*co*-glycolic acid) (PLGA) with L:G molar ratio of 85:15 (Sigma Aldrich, St. Louis, MO, USA) at 7% w/v of dichloromethane (DCM) (Tedia Co., Fairfield, OH, USA) and Paclitaxel (Bristol-Myers Squibb, U.K) at 20% w/w of PLGA. An Ultrasonicator (Cole-Parmer Instrument Co., IL, USA) was used to dissolve the components of the mixture homogeneously for about 15 min.

Mathematical Model

There is currently no single commercial software that is able to simulate all the physical processes that are important in EHDA fabrication of particles. These include the electric field, fluid flow field and processes relating to droplet formation, solvent evaporation and particle transport. Some software such as COMSOL can be used to solve for the electric field but not the particle trajectories. FLUENT can be used to handle free surface problems and particle trajectory calculations, but not electric field simulations. In this study, COMSOL 3.4 was used for simulating electric field and electric potential profiles without consideration of the effect of charged particles. The commercial CFD package GAMBIT 2.4 and FLUENT 6.3 (Ansys, Inc.) was used for simulating the EHDA process with consideration of the effect of space charge density.

Geometry and mesh

The geometry of the EHDA chamber as well as the operating parameters applied in the simulations conducted in this study followed that used in the experiments as discussed in the previous section so as to have a good basis for comparison. Following experimental observations, liquid droplets of different sizes were defined to be injected from the tip of the nozzle. The Rosin-Rammler diameter distribution method, with maximum droplet size of 12 μm and minimum droplet size of 6 μm, was used to define the droplet-size distribution. In addition, the solid-cone injection type was employed to define particle streams. The nitrogen inlet and outlet were defined to be opened to the surroundings at room temperature and 1 atm pressure. Two types of mesh, quadrilateral and triangular, for the interior and near-wall regions of the domain were applied, respectively. In total, 2796 and 1925814 computational cells were generated for the entire geometry in COMSOL and GAMBIT, respectively. The observed difference in total number of computational cells generated for simulations using COMSOL and FLUENT stemmed from the fact that the simulations carried out using FLUENT were three-dimensional (3-D), but those carried out using COMSOL were 2-D.

Computational fluid dynamics

The motion of the continuum gas phase is governed by the Navier-Stokes equations assuming the gas to be an incompressible fluid

$$\frac{\partial \rho_f}{\partial t} + \nabla.(\rho_f \mathbf{u}_f) = 0 \tag{1}$$

$$\rho_f \frac{\partial \mathbf{u}_f}{\partial t} + \rho_f \mathbf{u}_f \cdot \nabla \mathbf{u}_f = -\nabla P - \nabla \cdot \underline{\underline{\tau}} + \rho_f \mathbf{g} \tag{2}$$

where ρ_f is the fluid density, $\mathbf{u}_f$ is the fluid velocity vector, P is pressure, $\underline{\underline{\tau}}$ is the viscous stress tensor, and $\mathbf{g}$ is gravitational

acceleration.

The standard k-ε turbulence model was employed to simulate the nitrogen flow in the chamber. The turbulence kinetic energy k, and its rate of dissipation ε, were obtained from the following transport equations[19]

$$\frac{\partial}{\partial t}(\rho_f k) + \frac{\partial}{\partial x_i}(\rho_f k u_i) = \frac{\partial}{\partial x_j}\left[\left(\mu + \frac{\mu_t}{\sigma_k}\right)\frac{\partial k}{\partial x_j}\right] + G_k + G_b - \rho\varepsilon - Y_M + S_k \quad (3)$$

$$\frac{\partial}{\partial t}(\rho_f \varepsilon) + \frac{\partial}{\partial x_i}(\rho_f \varepsilon u_i) = \frac{\partial}{\partial x_j}\left[\left(\mu + \frac{\mu_t}{\sigma_\varepsilon}\right)\frac{\partial \varepsilon}{\partial x_j}\right] + C_{1\varepsilon}\frac{\varepsilon_l}{k}(G_k + C_{3\varepsilon}G_b) - C_{2\varepsilon}\rho_f\frac{\varepsilon^2}{k} + S_\varepsilon \quad (4)$$

where μ is the fluid viscosity, G_k represents the generation of turbulence kinetic energy due to mean velocity gradients, G_b is the generation of turbulence kinetic energy due to buoyancy, Y_M represents the contribution of the fluctuating dilatation in compressible turbulence to the overall dissipation rate, $C_{1\varepsilon}$, $C_{2\varepsilon}$ and $C_{3\varepsilon}$ are constants, and σ_k and σ_ε are the turbulent Prandtl numbers for k and ε, respectively. S_k and S_ε are user defined source terms. The velocity component can be calculated using Reynolds decomposition[20] as follows

$$u_i = \bar{u}_i + u_i' \quad (5)$$

where $\bar{u}_i$ and u_i' are the mean and fluctuating velocity components. The turbulent (or eddy) viscosity, μ_t, is computed by combining k and ε as follows

$$\mu_t = \rho C_\mu \frac{k^2}{\varepsilon} \quad (6)$$

where C_μ is a constant. The model constants $C_{1\varepsilon}$, $C_{2\varepsilon}$, C_μ, σ_k and σ_ε have the following default values[21]

$$C_{1\varepsilon} = 1.44, C_{2\varepsilon} = 1.92, C_\mu = 0.09, \sigma_k = 1.0, \sigma_\varepsilon = 1.3 \quad (7)$$

Droplet Dynamics

The governing equation for the motion of liquid droplets is

$$\rho_d\left(\frac{4}{3}\pi R_d^3\right)\frac{d\mathbf{u}_d}{dt} = \frac{1}{2}C_D(\pi R_d^2)\rho_f(u_f - u_d)(\mathbf{u}_f - \mathbf{u}_d) + \frac{4}{3}\pi R_d^3(\rho_d - \rho_f)\mathbf{g} + \mathbf{F}_B \quad (8)$$

where ρ_d shows the droplet density, R_d is the droplet radius, $\mathbf{u}_b$ shows the droplet velocity vector, C_D is the drag coefficient, and $\mathbf{F}_B$ shows other body forces acting in the system. The first term on the right is the drag force acting on the droplet, the second term is the buoyancy force due to gravity, and the third term is the total of other body forces which includes electric forces for the EHDA process.

Nitrogen flow was regarded as an incompressible, steady and viscous flow. The droplet trajectories were computed using the discrete phase model (DPM). In this model, the equation of motion was solved by the Lagrangian approach where droplets were tracked by a stochastic (random walk) model.[19] The electrostatic force on the charged droplets due to space charge effects was incorporated into the FLUENT solver as a component of the droplet body force. The nitrogen flow and the droplet discrete phase could be modeled directly in FLUENT. On the other hand, the electric field formed by charged droplets is governed by the well-known Poisson's equation which is generally unavailable in most CFD software including FLUENT. Two dominant classes of entities contribute to the electric potential within the EHDA chamber. These include the charged moving droplets and stationary surfaces which are charged conductors. The electric potential due to the charged moving droplets could be obtained by numerically solving the Poisson's equation with the appropriate boundary conditions

$$\nabla^2\Phi = -\frac{\rho_q}{\varepsilon_0\varepsilon_r} \quad (9)$$

where Φ is electric potential, ε_0 is the permittivity of vacuum, ε_r is the relative permittivity of nitrogen, and ρ_q is the space charge density, which is the charge per unit volume present at each point within a system. The second type of entities within the EHDA chamber mentioned earlier included the nozzle, ring and collecting plate. In the presence of such entities only the overall electric potential is governed by the Laplace equation

$$\nabla^2\Phi = 0 \quad (10)$$

In general, the Poisson's equation has to be solved when both types of entities are present. The electric field vector $\mathbf{E}$, can then be calculated by taking the negative gradient of the electric potential

$$\mathbf{E} = -\nabla\Phi \quad (11)$$

The resulting electric potential will give rise to an electric force as follows

$$\mathbf{F}_E = \mathbf{E}.q \quad (12)$$

where q is the charge of a droplet. The electric force term is substituted into Eq. 8 as part of the body force term.

Droplet collision and breakup model

Droplet-droplet collisions occur during the atomization of a liquid jet. For some applications, accounting for these collisions may be important in reproducing observed mean droplet sizes downstream of primary atomization.[22] The droplet collision algorithm of O'Rourke[23] is currently the standard approach for calculating collisions in Lagrangian spray simulations. This algorithm has a cost proportional to the square of the number of computational droplets, or "parcels." The droplet collision model suggested by O'Rourke was employed to calculate collision and coalescence among the dispersed liquid phase. The collision routine was operated for a pair of particles if, and only if, they were in the same computational cell. However, it may be noted that collisions between droplets are unlikely to occur in the current system due to presence of mutual repulsion between droplets arising from their equal polarity. Nevertheless, the collision model that is available in FLUENT had been included in the simulations to handle the unlikely event of droplets colliding due to strong aerodynamic forces that are able to overcome space charge forces. The frequency of occurrence of such collision events is not expected to be high and has not been analyzed in this study. In this collision model, the collision

probability was assumed to follow a Poisson distribution[24] based on a collision frequency and the computational time step. Using the probability information, the collision impact parameters were stochastically calculated.[25] The droplet collision algorithm of O'Rourke is available in FLUENT. When two parcels of droplets collide, the algorithm determines the type of collision and whether coalescence or bouncing occurs. The probability of each outcome is calculated from the droplet Weber number (We_d), and a fit to experimental observations. The droplet Weber number which compares the inertia to the surface tension forces is as follows[26]

$$We_d = \frac{\rho_d |\vec{v}_1 - \vec{v}_2|^2 \bar{d}}{\sigma} \tag{13}$$

where ρ_d and σ are the droplet density and surface tension, respectively, $\vec{v}_1$ and $\vec{v}_2$ are the velocities of the larger and smaller droplets, respectively, and $\bar{d}$ is the arithmetic mean diameter of the two parcels.

When droplet oscillations grow to a critical value the "parent" droplet will breakup into a number of smaller droplets. This Taylor analogy breakup (TAB) model[22] was used to model droplet breakup in this study. The model assumed a direct analogy between an oscillating and distorting droplet and a spring-mass system. It is recommended for low-Weber-number injections and is well suited for low-speed sprays into a standard atmosphere. It may also be noted at this point that the frequency of occurrence of droplet breakup in the current system is not expected to be high. Nevertheless the droplet breakup model was included in the simulations carried out due to the presence of low-Weber number within the system.

Electric force model

The generic force equation in FLUENT is exactly identical to the acceleration equation presented in Eq. 8 with the substitution of Eq. 12, but for unit droplet mass as follows

$$\frac{d\mathbf{u}_d}{dt} = \frac{3C_D \mu \mathrm{Re}}{8R_d^2 \rho_d}(\mathbf{u}_f - \mathbf{u}_d) + \frac{(\rho_d - \rho_f)}{\rho_d}\mathbf{g} + \mathbf{E}.q_m \tag{14}$$

where $\mathrm{Re} = \frac{2R_d(\rho_d - \rho_f)(u_f - u_d)}{\mu}$ and $q_m = \frac{q}{\rho_d(\frac{4}{3}\pi R_d^3)}$ is the charge-to-mass ratio of an individual droplet. The arbitrary body force term ($\mathbf{E}.q_m$) can be altered using the "User Defined Functions" module in FLUENT. For an arbitrary scalar $\mathbf{\Phi}_k$, the user-defined scalar transport equation in FLUENT has the following form

$$\frac{\partial \rho \mathbf{\Phi}_k}{\partial t} + \nabla(\rho \mathbf{u} \mathbf{\Phi}_k - \Gamma \nabla \mathbf{\Phi}_k) = S_{\Phi k} \tag{15}$$

where Γ and $S_{\Phi k}$ are the diffusion coefficient and source term, respectively, while the second term (leftmost in the bracket) represents convective flux of the scalar $\mathbf{\Phi}_k$. Since steady-state simulations were carried out, the first term on the lefthand side of the transport equation was automatically zero. In order to modify the transport equation into the Laplace equation, the convective flux term must be disabled. In addition, ε_0 should be used as the value for $\mathbf{\Gamma}$. Last, the source term was set to zero. In order to change from the Laplace equation to the Poisson's equation, the source term of the transport equation must be given the value of the space charge density. For a droplet with a constant charge-to-mass ratio, the method of implementation of space charge in FLUENT may be used.[11]

Table 1. Physical Properties of DCM+PLGA Solution Used for Calculation of Doplet Diameter and Current[16]

Physical property	Value
Density of DCM+PLGA (7% w/v) (kg/m^3)	1376
Electrical conductivity of DCM+PLGA (7% w/v) (S/m)	1.5×10^{-8}
Surface tension of pure DCM (N/m)	4.4×10^{-4}
Electrical permittivity of vacuum (C^2/N m^2)	8.85×10^{-12}

The concentration of droplets simulated with DPM was calculated by the following equation when simulations were performed with coupled interactions between the fluid and droplet phases[27]

$$C = \frac{1}{\delta_v}\sum \dot{m}(t_{\mathrm{out}} - t_{\mathrm{in}}) \tag{16}$$

where δ_v is the volume of a computation cell, $\dot{m}$ is the mass flow rate of a droplet stream passing through the cell, and t_{in} and t_{out} denote the time that the droplet stream enters and exits the cell, respectively. In FLUENT, the droplet concentration in a cell is defined as the total mass of discrete phase in the cell divided by the volume of the cell. In steady-state modeling, the total mass of droplets entering a cell is equal to the mass of droplets leaving the cell. So no cell will accumulate any droplets. The droplet concentration is calculated based on the droplet residue time in each cell. By replacing $\dot{m}$ with the charge flow rate of a droplet stream I_d, the expression for the space charge density can be calculated as follows

$$S_{\Phi k} = \frac{1}{\delta_v}\sum I_d(t_{\mathrm{out}} - t_{\mathrm{in}}) \tag{17}$$

User defined function codes written in C^{++} were used to implement Poisson field analysis for droplets with varying charge-to-mass ratios.

Initial conditions for particle trajectory simulations

Following Ganan-Calvo,[28] initial diameter d_d of the droplet formed by EHDA, and the total current I generated by the process could be empirically correlated to the EHDA solution flow rate Q, and solution properties using dimensionless quantities[16]

$$\frac{d_d}{d_0} = 0.092\left(\frac{Q}{Q_0}\right)^{1/2} - 0.01 \tag{18}$$

$$\frac{I}{I_0} = 2.4\left(\frac{Q}{Q_0}\right)^{1/4} + 1.72 \tag{19}$$

where d_0, I_0, and Q_0 are the reference values for droplet diameter, current and solution flow rates, respectively. These were based on the relationships by Gavan-Calvo and have the following expressions[28]

$$Q_0 = \gamma\varepsilon_0/\rho K, \quad I_0 = \left(\gamma^2\varepsilon_0/\rho\right)^{1/2}, \quad d_0 = \left[\gamma\varepsilon_0^2/\left(\rho K^2\right)\right]^{1/3} \tag{20}$$

where ρ and K are the density and electrical conductivity of the polymeric solution, and γ is the gas-liquid surface tension. The physical properties of DCM+PLGA (7% w/v) are tabulated in Table 1.

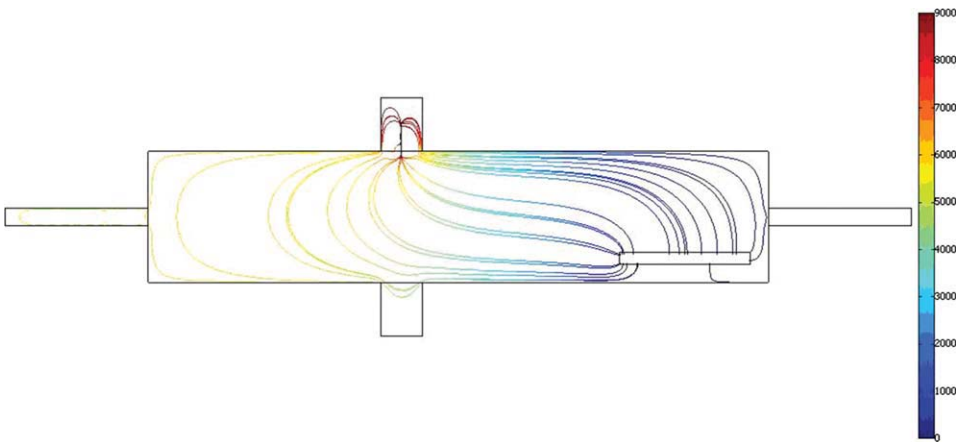

Figure 3. Electric field lines (V/m) in the computational domain obtained from CFD simulations carried out using COMSOL with the following conditions: nozzle voltage 9 kV and ring voltage 6 kV.

[Color figure can be viewed in the online issue, which is available at wileyonlinelibrary.com.]

The ratio of droplet diameter to jet diameter could be obtained.[29] Using this ratio, the initial particle velocity was estimated by dividing the polymeric solution flow rate by the cross-sectional area of the jet. In the simulations carried out in this study, this ratio was used for estimating the initial velocity of droplets. This estimated velocity was then used as an initial guess for starting the simulations.

Solvent evaporation from droplets

For simplicity, the internal diffusion of DCM and PLGA within the droplets was ignored. Instead, simulations were carried out assuming particles to be bicomponent with 7 wt % PLGA and the rest DCM. Particles were assumed to be perfectly well mixed throughout the simulation, and the density of the particle was computed by volume addition using the densities of pure DCM and PLGA.

The rate of evaporation of DCM vapor from the droplet's surface was computed using the Sherwood number correlation[30–31]

$$\mathrm{Sh}_{AB} = \frac{k_c d_d}{D_{i,m}} = 2.0 + 0.6\mathrm{Re}_d^{1/2}\mathrm{Sc}^{1/3} \tag{21}$$

where $D_{i,m}$ is the diffusion coefficient of vapor in the bulk (m^2/s), k_c is the mass-transfer coefficient (m/s), and Sc is the Schmidt number $\frac{\mu}{\rho D_{i,m}}$. The partial pressure of DCM vapor at the particle's surface was obtained by Raoult's law. To obtain the convective mass-transfer coefficient from the Sherwood number, the diffusion coefficient of DCM in nitrogen gas was required as a material property input. Since nitrogen is nonpolar, and DCM has a small dipole moment, the Hirschfelder's equation[32] was used to calculate the diffusion coefficient of DCM vapor in nitrogen

$$D_{\mathrm{DCM,N_2}} = \frac{0.001858T^{3/2}\left[\frac{1}{M_{DCM}} + \frac{1}{M_{N_2}}\right]^{1/2}}{P\sigma^2_{\mathrm{DCM,N_2}}\Omega_D} \tag{22}$$

where $D_{\mathrm{DCM,N_2}}$ is the mass diffusivity of DCM vapor through nitrogen (m^2/s), T is the absolute temperature (K), M is the molecular weight, P is the absolute pressure (atm), σ is the "collision diameter" (angstrom), and Ω_D is the "collision integral" for molecular diffusion, a dimensionless function of temperature and of the intermolecular potential field for one molecule of A and one molecule B. Therefore, the mass of the droplet is reduced according to

$$m_d(t + \Delta t) = m_d(t) - N_{DCM}A_d M_{DCM}\Delta t \tag{23}$$

where m_d is mass of the droplet (kg), A_d is surface area of the droplet (m^2), and N_{DCM} is molar flux of DCM vapor which can be calculated as follows

$$N_{DCM} = k_c(C_{DCM,s} - C_{DCM,\infty}) \tag{24}$$

where $C_{DCM,s}$ is DCM vapor concentration at the droplet surface ($kgmol/m^3$), and $C_{DCM,\infty}$ is DCM vapor concentration in the bulk gas ($kgmol/m^3$).[30–31] FLUENT solves Eq. 24 in conjunction with the equivalent heat-transfer equation using a stiff coupled solver.

Boundary Conditions

The boundary conditions of the user-defined scalar that represented electric potential were as follows. All surfaces of the nozzle were set at a constant value (7 kV–9 kV), the ring surface was set at a constant value (5 kV–7 kV), surfaces of the collecting plate were set at a constant value of

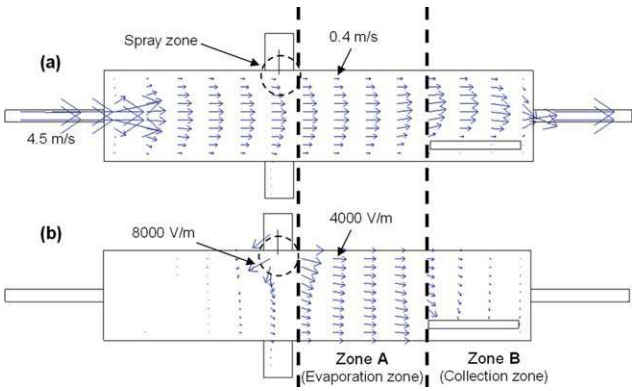

Figure 4. (a) Flow field within the chamber for 35 L/min nitrogen flow rate, and (b) electric field within the chamber for 9 kV nozzle voltage and 6 kV ring voltage.

[Color figure can be viewed in the online issue, which is available at wileyonlinelibrary.com.]

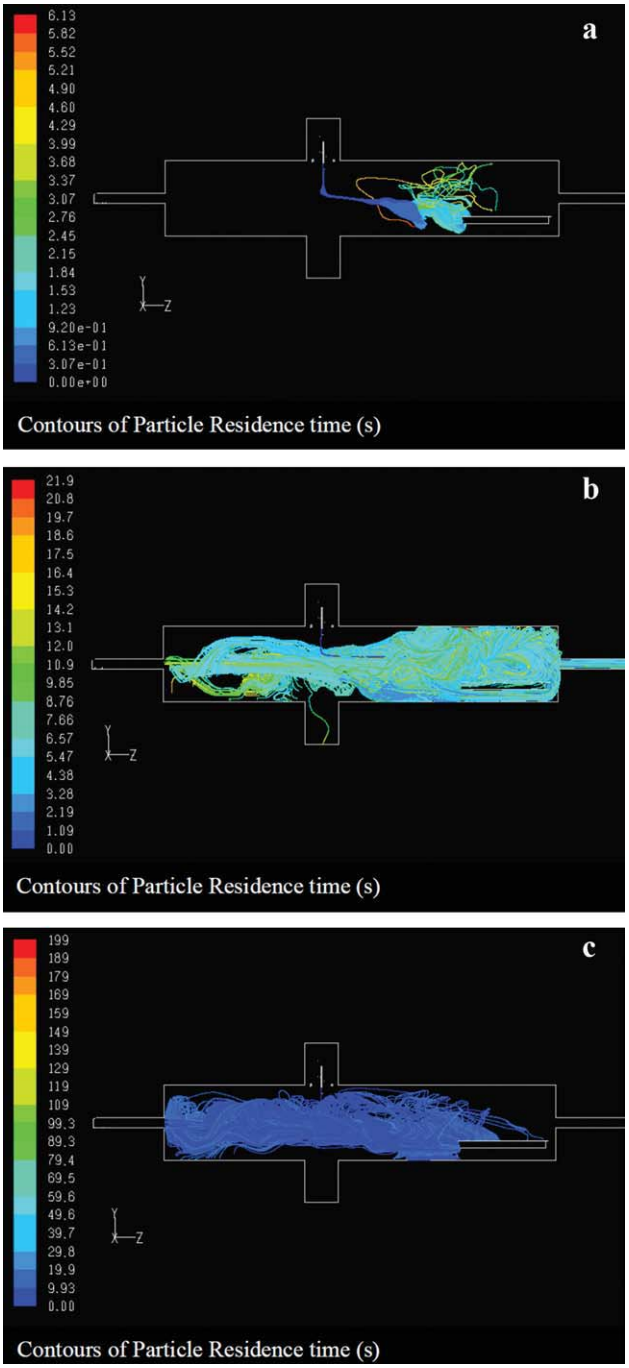

Figure 5. Particle residence time profiles in the computational domain obtained from the CFD simulations with the following conditions: (a) Solution flow rate 1.0 mL/h, nitrogen flow rate 35 L/min, voltage difference between nozzle and ring 3 Kv, (b) solution flow rate 2.5 mL/h, nitrogen flow rate 25 L/min, voltage difference between nozzle and ring 2 kV, and (c) solution flow rate 2.5 mL/h, nitrogen flow rate 20 L/min, voltage difference between nozzle and ring 1 kV.

[Color figure can be viewed in the online issue, which is available at wileyonlinelibrary.com.]

zero, and the flux of the user-defined scalar normal to each of the remaining surfaces were set to zero. In this manner, the chamber's walls, inlet and outlet were treated as insulators. All surfaces were set to be isothermal at 300 K. Solid particles were defined to be trapped only at the collecting surface. Due to solvent evaporation, droplets reduced in size rapidly and were converted to solid particles after a very short period of time. Solid particles and liquid droplets were recognized as "escaped" when they touched the ring, nozzle, chamber walls and the inlet or outlet. A "trapped" status meant that all DCM still present within the droplet would automatically vaporize once the solid particle reached the collecting surface. This is to allow easy computation of particle collection efficiency (CE) as

$$\mathrm{CE} = \frac{\mathrm{Trapped}}{\mathrm{Trapped} + \mathrm{Escaped} + \mathrm{Incomplete}} \times 100 \qquad (25)$$

The "incomplete" status referred to solid particles or liquid droplets which are still moving through the chamber and have not been deposited yet.

Results and Discussion

In this section, typical scalar and vector field distributions, such as electric potential, nitrogen velocity and particle residence time will be presented to illustrate results obtained from the CFD simulations.

Electric field distribution

Figure 3 shows the electric field lines in the Y-Z plane of the computational domain obtained from the CFD simulations carried out using COMSOL. It may be seen that the electric field lines which are perpendicular to electric potential lines emanate from the tip of the needle and end on the collecting plate. It seems that the most important factor affecting the electric field distribution is the voltage difference between the spray zone and the collecting plate, while space-charge density does not have a considerable effect on the electric potential profile. In view of the applied solution flow rates, the concentration of liquid droplets in space is very low. This very dilute system of charged species in a voluminous space results in a low space-charge density which does not influence the electric field distribution within the chamber significantly. Therefore, the most important factors influencing the electric field distribution inside the chamber are nozzle and ring voltages as well as the distance between the spray zone and the collecting plate.

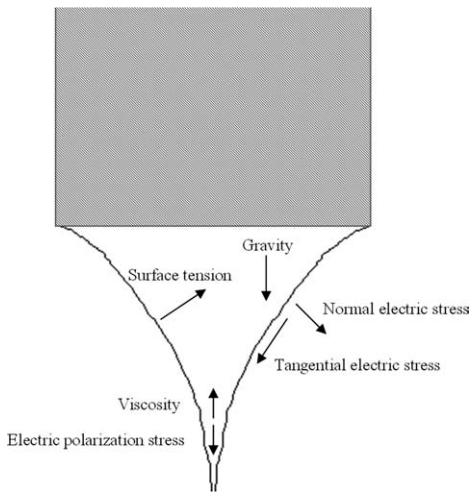

Figure 6. Forces acting on the Taylor cone in the EHDA process.[3]

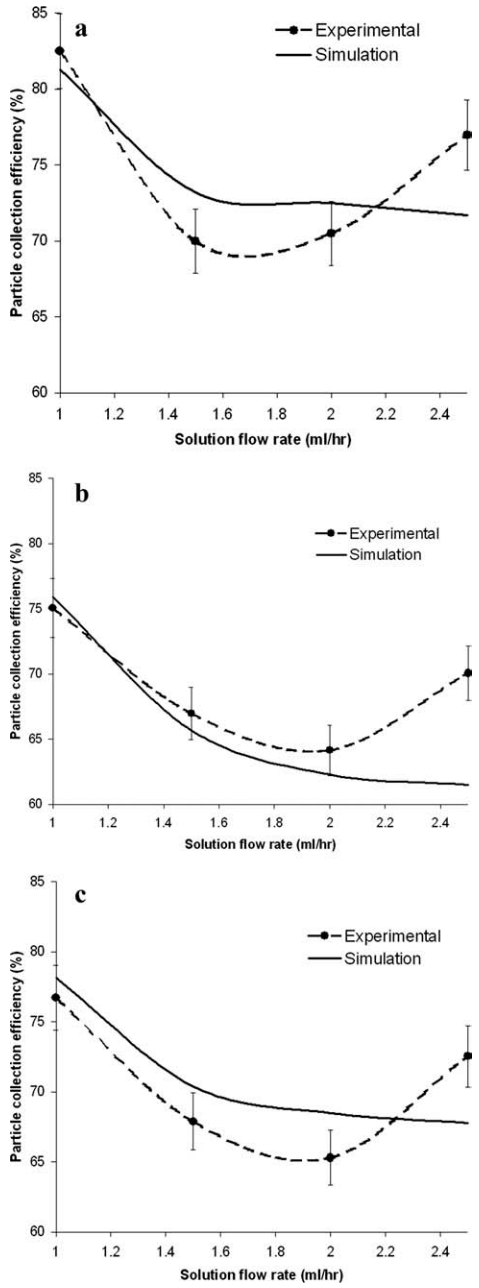

Figure 7. Comparisons of particle collection efficiency variations with solution flow rate obtained experimentally with CFD simulations under the following conditions: nozzle voltage 9 kV.

(a) nitrogen flow rate 35 L/min, voltage difference between nozzle and ring 3.5 kV, (b) nitrogen flow rate 25 L/min, voltage difference between nozzle and ring 3 kV, and (c) nitrogen flow rate 20 L/min, voltage difference between nozzle and ring 2 kV.

Particle residence time

The residence time for charged particles moving in the chamber depends on the electric field and flow field inside the chamber. Figure 4 shows that three distinct zones can be observed within the chamber. These comprise first a spray zone which includes the nozzle and the ring where solution injection, atomization, droplet collision and breakup occur. Second, there is an evaporation zone (zone A) in which solvent is evaporating from the droplets and particles are traveling toward the collecting plate. Last, there is a collection zone (zone B) in which solid particles are either deposited on the collecting plate or traveling toward the outlet. Figure

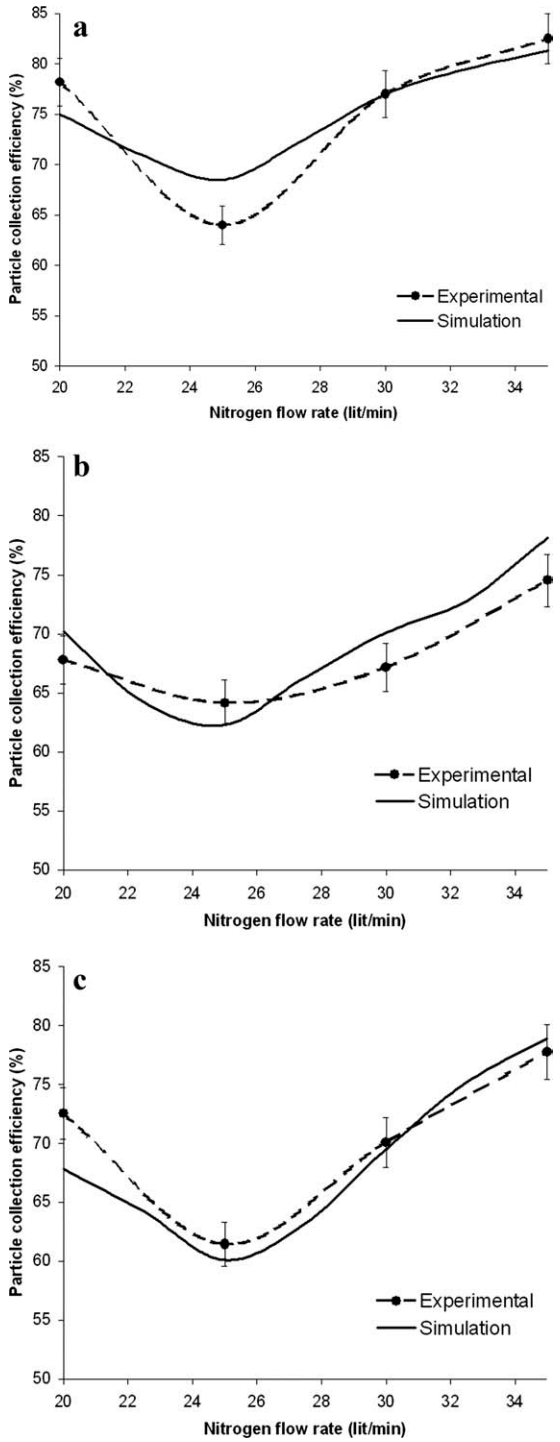

Figure 8. Comparisons of particle collection efficiency variations with nitrogen flow rate obtained experimentally with CFD simulations under in the following conditions: nozzle voltage 9 kV.

(a) solution flow rate 1.0 mL/h, voltage difference between nozzle and ring 3.5 kV, (b) solution flow rate 2.0 mL/h, voltage difference between nozzle and ring 3 kV, and (c) solution flow rate 2.5 mL/h, voltage difference between nozzle and ring 2 kV.

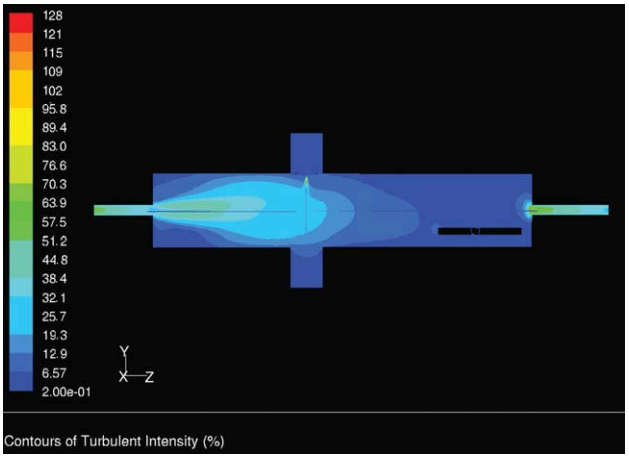

Figure 9. Turbulence intensity in the EHDA chamber at nitrogen flow rate of 25 L/min.

[Color figure can be viewed in the online issue, which is available at wileyonlinelibrary.com.]

4 shows that the general direction of the electric field (and, therefore, the electric force) is toward the collecting plate. On the other hand, the general direction of the flow field (and, therefore, the drag force) is toward the outlet. In zone A, these two types of forces are aligned generally in the same direction. Therefore, both the drag force and electric force in zone A complement each other to transport particles toward the collecting plate. Conversely, in zone B the drag force and electric force are aligned in different directions. The drag force is directed toward the outlet, while the electric force is directed toward the collecting plate. Thus, if the drag force is larger than the electric force in zone B, particles would tend to travel toward the outlet. On the other hand, particles would tend to deposit on the collecting plate if the electric force is dominant in the collection zone.

Figures 5a, b and c show the particle residence time profiles in the Y-Z plane of the computational domain obtained from the FLUENT simulations. It may be seen that the particle residence time is related to the solution flow rate, nitrogen flow rate and voltage difference between the nozzle and ring. It is observed that with increasing solution flow rate, decreasing nitrogen flow rate and voltage difference between the nozzle and ring, the particle residence time increased from 3 s in Figure 5a to 7 s in Figure 5b, and more than 10 s in Figure 5c. The most important factor in determining the electric field in the EHDA process would be the voltage difference between the ring and nozzle.[1] The spray mode could be changed from multiple spray cone to single spray cone and finally to the dripping mode with decreasing voltage difference between the ring and nozzle.[17] The dripping mode appears when the voltage difference is small, and this can cause a significant impact on collection efficiency. In other words, voltage difference between nozzle and ring has a significant effect on the jet formation process,[14–15,33] which in turn affects the particle residence time and collection efficiency.

Figure 5a shows that the number of particles within the chamber is small due to a relatively low-solution flow rate. The electric force is dominant due to a high-voltage difference applied between the nozzle and ring and this has resulted in higher particle collection efficiency. In Figure 5b, the number of particles is larger due to a higher solution flow rate. The particle residence time is higher due to a lower nitrogen flow

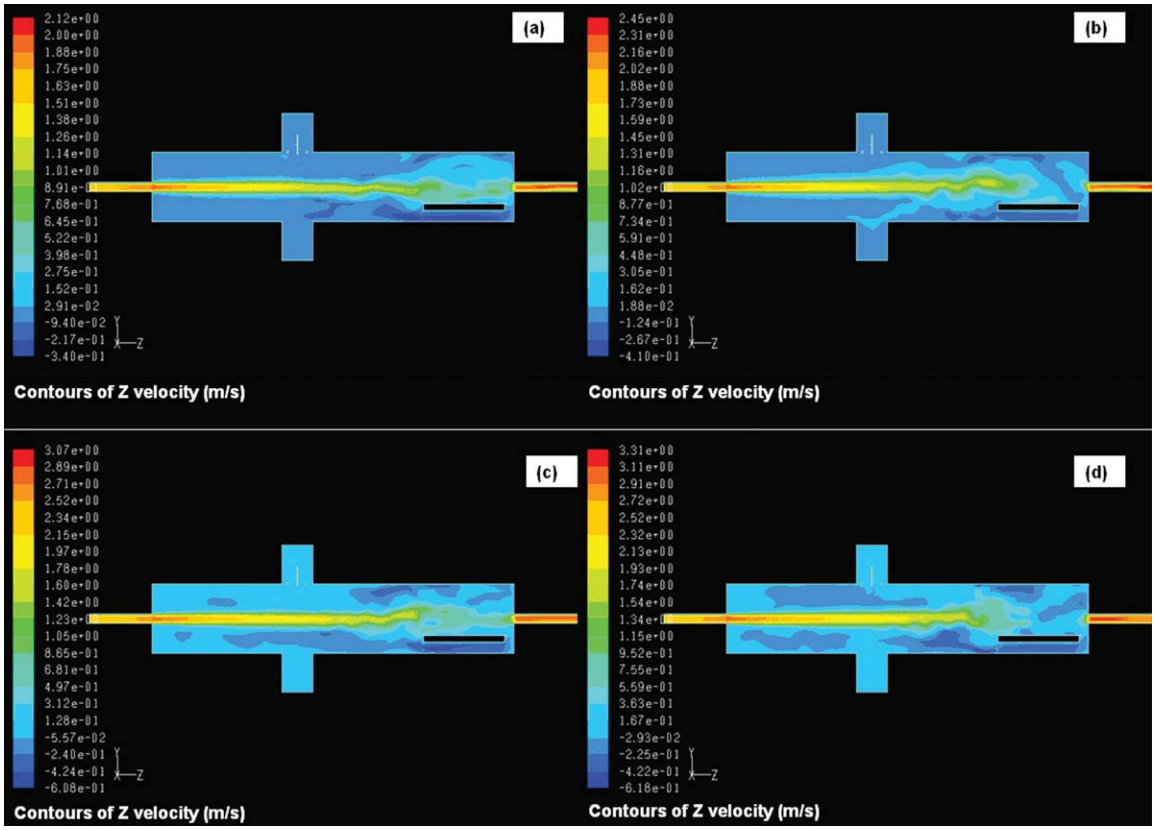

Figure 10. Velocity contours for nitrogen flow rates of (a) 20 L/min, (b) 25 L/min, (c) 30 L/min, and (d) 35 L/min.

[Color figure can be viewed in the online issue, which is available at wileyonlinelibrary.com.]

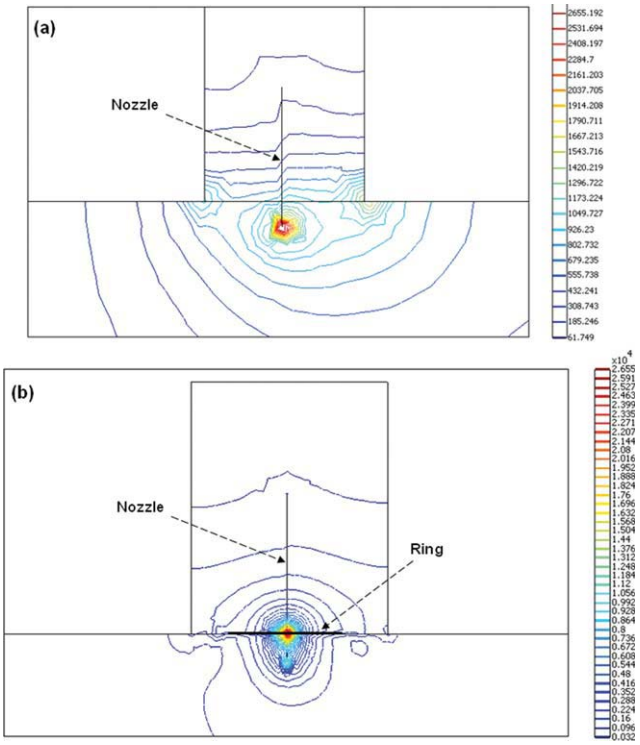

Figure 11. (a) Electric field profile for 9 kV nozzle voltage, and (b) electric field profile for 9 kV nozzle voltage and 6 kV ring voltage.

[Color figure can be viewed in the online issue, which is available at wileyonlinelibrary.com.]

rate used. In the collection zone, due to comparable magnitudes of the electric force and the drag force resulting from the smaller voltage difference applied, the particle collection efficiency achieved is lower. Finally in Figure 5c, the number of particles is large due to a high solution flow rate. However, due to a low-voltage difference between the nozzle and ring, the electric force is now dominated by the drag force and this leads to a large number of particles being transported out of the chamber through the outlet and, consequently, much lower particle collection efficiency.

Operational parameters

In this section, the effect of three operational parameters including solution flow rate, nitrogen flow rate and voltage difference between the nozzle and ring on particle collection efficiency will be presented. In addition, experimental results will be compared with the results of CFD simulations.

Solution flow rate

Figure 6 shows the various forces exerted on the Taylor cone formed at the tip of the nozzle in the EHDA process. In the Taylor cone at the tip of the nozzle, charges are transported in two ways. The first is by charge conduction in the liquid due to the electric fields and the second is by charge convection. The electric field accelerates charges at the liquid surface to the tip of the cone and these charges in turn accelerate the surrounding liquid by their motions.[3] The electric field and free electric charges induced by this electric field create a normal electric stress at the liquid surface. These free charges also experience a force at the air-liquid interface which is known as the tangential electric stress. Another electrical stress known as polarization stress is the normal stress acting on the liquid when the liquid is

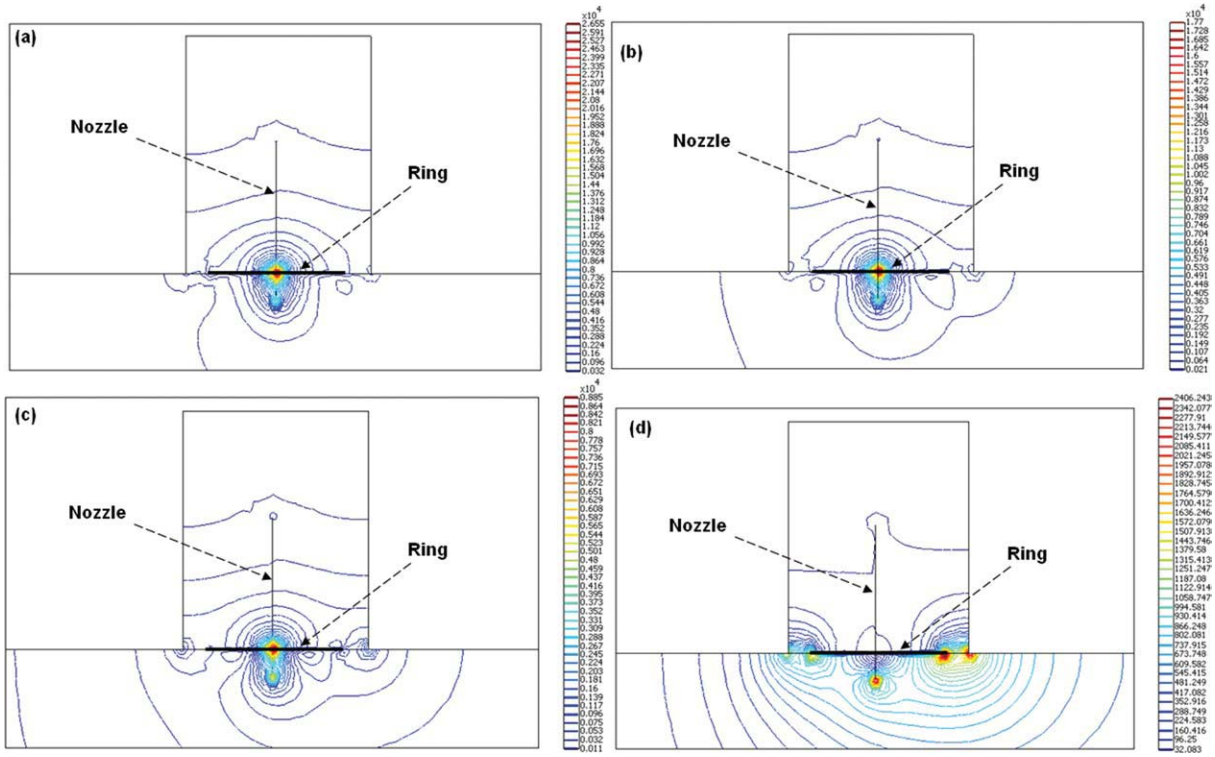

Figure 12. Electric field profile (shown by electric field contours in V/m) with 9 kV nozzle voltage (a) 6 kV ring voltage, (b) 7 kV ring voltage, (c) 8 kV ring voltage, and (d) 9 kV ring voltage.

[Color figure can be viewed in the online issue, which is available at wileyonlinelibrary.com.]

polarized by the electric field. Surface tension stress can be defined as the pressure difference due to surface tension between the liquid and the surrounding air. Viscous surface stress is also present within the accelerating liquid.[3] It may be noted that although these various stresses are present in an actual physical system such as the EHDA experiments conducted in this study, they have not been considered in the simulations carried out for sake of computational efficiency. This may account for quantitative differences between experimental and simulation results obtained as will be discussed next. Figure 7 shows the variations of particle collection efficiency with solution flow rate obtained from experiments and simulations. Quantitative differences between experimental and simulation results may be observed for solution flow rates higher than 2 mL/h. This discrepancy may be attributed to instability observed in the Taylor cone[34] in the experiments conducted which has not been addressed in the simulations.

Nitrogen flow rate

Figure 8 shows variations of particle collection efficiency with nitrogen flow rate obtained from experiments and simulations. In comparison with Figure 7, the agreement in particle collection efficiencies obtained experimentally and computationally at different nitrogen flow rates is better. In general, an increase in nitrogen flow rate increases the magnitudes of drag forces. However, at low-nitrogen flow rates the effects due to increasing turbulence intensities within the chamber may be more significant than increasing magnitudes of drag forces. Figure 9 shows that turbulence intensities of more than 40% could be observed in large parts of the chamber. Under such conditions, an increasing nitrogen flow rate has the undesirable effect of enhancing turbulence intensities to a greater extent than drag forces and this leads to a higher likelihood of particles being deposited on the walls of the EHDA chamber. This accounts for the inverse relation between particle collection efficiency and nitrogen flow rate at low-flow rates observed in both experiments and simulations. The converse is true at high-nitrogen flow rates. Figure 10 shows that the axial component of nitrogen velocity within the chamber increases significantly with increasing inlet flow rate. This is expected to enhance the effects of drag on particles formed and, thus, aid in the transport of particles to the collecting plate.

Voltage difference between nozzle and ring

Experimental results have confirmed that particle collection efficiency changes gradually with separate variations in the nozzle and ring voltages. The particle collection efficiency is not strongly influenced by the nozzle voltage or ring voltage separately because the combined nozzle and ring system allows the formation of a single-cone-jet over a wide range of voltage differences.[18] When a single-nozzle electrode is used instead, the range of permitted voltages for the formation of the cone-jet is usually very small. Figure 11 shows the effect of ring voltage on the electric field profile in the spray zone. This figure confirms that the ring voltage has a considerable effect on electric field strength in the spray zone. Electric field lines in the spray zone are much more concentrated in Figure 11b, and the magnitude of the electric field is also much higher in comparison to Figure 11a. Therefore, it can be concluded that using a metal ring with a lower voltage around the nozzle results in a stronger electric field in the spray zone. A stronger electric field in the chamber results in stronger electric forces. It was illustrated in Figure 4 that dominance of the electric force, especially in the collection zone, has a positive effect on particle collection efficiency.

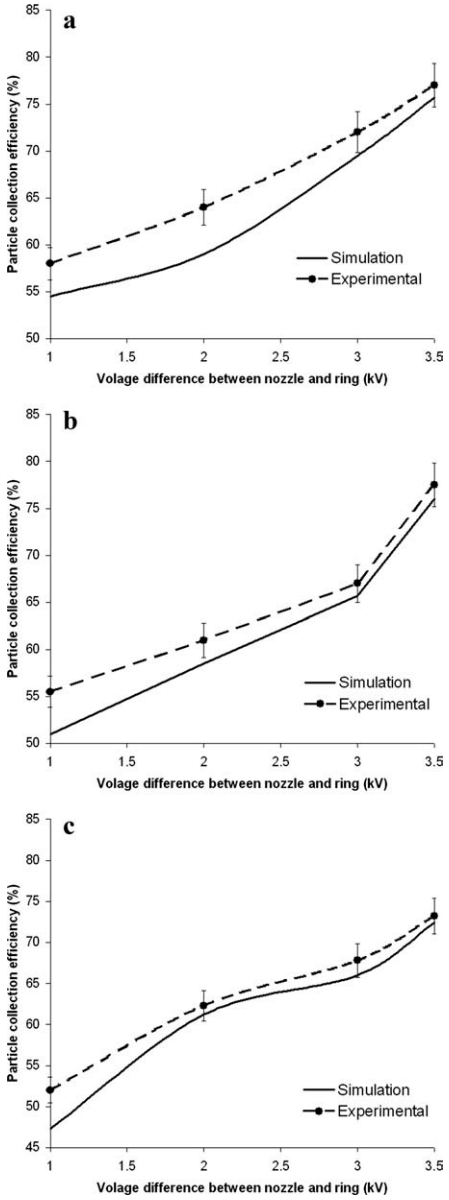

Figure 13. Comparisons of particle collection efficiency variations with voltage difference between nozzle and ring obtained experimentally with CFD simulations under the following conditions: Nozzle voltage 9 Kv; (a) solution flow rate 2.5 mL/h, nitrogen flow rate 35 L/min, (b) solution flow rate 2.0 mL/h, nitrogen flow rate 30 L/min, and (c) solution flow rate 1.5 mL/h, nitrogen flow rate 25 L/min.

On the other hand, the experimental results obtained in previous studies had shown that the voltage difference between the nozzle and ring had considerable effects on the morphology of the fabricated particles, as well as particle collection efficiency.[17–18] This effect can also be related to the strength of the electric field. Figure 12 shows the effect of voltage difference between the nozzle and ring on the

strength of the electric field. In Figure 12a the strongest electric field can be observed with a ring voltage of 6 kV. The strength of the electric field decreases with increasing ring voltage and decreasing voltage difference between the nozzle and ring. Figure 13 shows that higher particle collection efficiencies are indeed achieved in both the experiments and simulations conducted at higher voltage differences between the nozzle and ring.

Conclusions

A computational model was developed in this study to simulate the fluid and particle dynamics in an EHDA chamber. Such a model has the potential to be used for predicting particle collection efficiencies of particle fabrication processes using the EHDA methodology under different operating conditions. Experiments have also been conducted in this study using a new design for the EHDA chamber. The particle residence time within the EHDA chamber could be increased by increasing the solution flow rate, decreasing the nitrogen flow rate and applying a smaller voltage difference between the nozzle and ring. The effect of nitrogen flow rate on particle collection efficiency was investigated both experimentally and computationally. Within the range of flow rates considered, particle collection efficiency profiles exhibited minimum points due to the presence of two opposing factors relating to magnitudes of drag forces and turbulence intensities present during the EHDA process. Higher particle collection efficiencies were also achieved at higher voltage differences between the nozzle and ring due primarily to the presence of a stronger electric field within the EHDA chamber under such conditions.

Acknowledgments

This project is supported by the Biomedical Research Council, A*STAR under the grant number 07/1/21/19/508. We would like to thank Lee, Teng Yong Jeffrey for his technical support on this work.

Literature Cited

1. Almekinders JC, Jones C. Multiple jet electrohydrodynamic spraying and applications. *J Aerosol Sci*. 2003;30:969–971.
2. Tatemoto Y, Ishikawa R, Takeuchi M, Takeshita T, Noda K, Okazaki T. An electrospray method using a multi-capillary nozzle emitter. *Chem Eng Tech*. 2007;30:1274–1279.
3. Hartman RPA, Brunner DJ, Camelot DMA, Marijnissen JCM, Scarlett B. Electrohydrodynamic atomization in the cone-jet mode: physical modeling of the liquid cone and jet. *J Aerosol Sci*. 1999; 30:823–849.
4. Hayati I, Bailey A, Tadros THF. Investigations into the Mechanisms of Electrohydrodynamic Spraying of Liquids: 1. Effect of electric field and the environment on pendant drops and factors affecting the formation of stable jets and atomization. *J Colloid Interface Sci*. 1987;117:205–221.
5. Barrero A, Ganan-Calvo AM, Fernandez-Feria R. The role of liquid viscosity and electrical conductivity on the motions inside Taylor cones in E.H.D. spraying of liquids. *J Aerosol Sci*. 1996;27:175–176.
6. Farook U, Zhang HB, Edirisinghe MJ, Stride E, Saffari N. Preparation of microbubble suspensions by co-axial electrohydrodynamic atomization. *Med Eng Phys*. 2007;29:749–754.
7. Lopez-Herrera JM, Ganan-Calvo AM, Perez-Saborid M. One-dimensional simulation of the breakup of capillary jets of conducting liquids: application to EHD spraying. *J Aerosol Sci*. 1999;30:895–912.
8. Lastowa O, Balachandran W. Novel low voltage EHD spray nozzle for atomization of water in the cone jet mode. *J Electrostatics*. 2007;65:490–499.
9. Noymer PD, Garel M. Stability and atomization characteristics of electrohydrodynamic jets in the cone-jet and multi-jet modes. *J Aerosol Sci*. 2000;31:1165–1172.
10. Ragucci R, Fabiani F, Cavaliere A, Muscetta P, Noviello C. Characterization of stability regimes of electrohydrodynamically enhanced atomization. *Exp Therm Fluid Sci*. 2000;21:156–161.
11. Zhao SX, Adamiak K, Peter Castle GS. The implementation of poisson field analysis within fluent to model electrostatic liquid spraying. *Canadian Conference on Electrical and Computer Engineering*. 2007; 1456–1459.
12. Lastowa O, Balachandran W. Numerical simulation of electrohydrodynamic (EHD) atomization. *J Electrostatics*. 2006;64:850–859.
13. Hong Y, Li Y, Yin Y, Li D, Zou G. Electrohydrodynamic atomization of quasi-monodisperse drug-loaded spherical/wrinkled microparticles. *J Aerosol Sci*. 2008;39:525–536.
14. Xie J, Marijnissen JCM, Wang CH. Microparticles developed by electrohydrodynamic atomization for the local delivery of anticancer drug to treat C6 glioma in vitro. *Biomaterials*. 2006;27:3321–3332.
15. Xie J, Wang CH. Electrospray in the dripping mode for cell microencapsulation. *J. Colloid Interface Sci*. 2007;312:247–255.
16. Yao J, Lim LK, Xie J, Hua J, Wang CH. Characterization of electrospraying process for polymeric particle fabrication. *J Aerosol Sci*. 2008;39:987–1002.
17. Ding L, Lee T, Wang CH. Fabrication of monodispersed Taxol-loaded particles using electrohydrodynamic atomization. *J Controlled Release*. 2005;102:395–413.
18. Xie J, Lim LK, Phua Y, Hua J, Wang CH. Electrohydrodynamic atomization for biodegradable polymeric particle production. *J Colloid Interface Sci*. 2006;302:103–112.
19. *FLUENT 6.3 User's Guide*. Fluent, Inc; 2006.
20. Bird RB, Stewart WE, Lightfoot EN. *Transport Phenomena*. New York: Wiley & Sons; 2002.
21. Launder BE, Spalding DB. *Lectures in Mathematical Models of Turbulence*. London, UK: Academic Press; 1972.
22. Yoon SS, Hewson JC, DesJardin PE, Glaze DJ, Black AR, Skaggs RR, Numerical modeling and experimental measurements of a high speed solid-cone water spray for use in fire suppression applications. *Int J Multiphase Flow*. 2004;30:1369–1388.
23. O'Rourke PJ. *Collective Drop Effects on Vaporizing Liquid Sprays*. New Jersey: Princeton University; 1981.
24. Gavaises M, Theodorakakos A, Rergeles G, Brenn G. Evaluation of the effect of droplet collisions on spray mixing. *Proc Inst Mech. Eng*. 1996;210:465–475.
25. Shang HM, Kim YM, Chen CP, Wang TS. Numerical studies of droplet-turbulence interactions. *Appl Math Comput*. 1994;65:63–78.
26. Shan Y, Coyle TW, Mostaghimi J. Numerical simulation of droplet breakup and collision in the solution precursor plasma spraying. *J Thermal Spray Technol*. 2007;16:698–704.
27. Ye Q, Steigleder T, Scheibe A, Domnick J. Numerical simulation of the electrostatic powder coating process with a corona spray gun. *J Electrostatics*. 2002;54:189–205.
28. Ganan-Calvo AM. The surface charge in electrospraying: its nature and its universal scaling laws. *J Aerosol Sci*. 1999;30:863–872.
29. Cloupeau M, Prunet-Foch B. Electrohydrodynamic spraying functioning modes: a critical review. *J Aerosol Sci*. 1994;25:1021–1036.
30. Ranz WE, Marshall WR. Evaporation from drops, Part I. *Chem Eng Prog*. 1952;48:141–146.
31. Ranz WE, Marshall WR. Evaporation from drops, Part II. *Chem Eng Prog*. 1952;48:173–180.
32. Welty JR, Wicks CE, Wilson RE, Rorrer G. *Fundamentals of Momentum, Heat and Mass Transfer*. New York, NY: John Wiley & Sons; 2001.
33. Nie H, Wang CH. Fabrication and characterization of PLGA/HAp composite scaffolds for delivery of BMP-2 plasmid DNA. *J Controlled Release*. 2007;120:111–121.
34. Grace JM; Marijnissen JCM. A review of liquid atomization by electrical means. *J. Aerosol Sci*. 1994;25:1005–1019.

Manuscript received Jun. 10, 2010, revision received Sept. 4, 2010, and final revision received Dec. 28, 2011.